



HAL
open science

Radiative Transfer For Variable 3D Atmospheres

François Golse, Frédéric Hecht, Olivier Pironneau, Didier Smets, Pierre-Henri Tournier

► **To cite this version:**

François Golse, Frédéric Hecht, Olivier Pironneau, Didier Smets, Pierre-Henri Tournier. Radiative Transfer For Variable 3D Atmospheres. *Journal of Computational Physics*, 2023, 475, pp.111864. 10.1016/j.jcp.2022.111864 . hal-03751448

HAL Id: hal-03751448

<https://hal.science/hal-03751448>

Submitted on 14 Aug 2022

HAL is a multi-disciplinary open access archive for the deposit and dissemination of scientific research documents, whether they are published or not. The documents may come from teaching and research institutions in France or abroad, or from public or private research centers.

L'archive ouverte pluridisciplinaire **HAL**, est destinée au dépôt et à la diffusion de documents scientifiques de niveau recherche, publiés ou non, émanant des établissements d'enseignement et de recherche français ou étrangers, des laboratoires publics ou privés.

Radiative Transfer For Variable 3D Atmospheres

Working Document to be submitted to JCP

F. Golse, F. Hecht, O. Pironneau, D. Smets and P.-H. Tournier

August 14, 2022

Abstract

To study the temperature in a gas subjected to electromagnetic radiations, one may use the Radiative Transfer equations coupled with the Navier-Stokes equations. The problem has 7 dimensions; however with minimal simplifications it is equivalent to a small number of integro-differential equations in 3 dimensions. We present the method and a numerical implementation using an \mathcal{H} -matrix compression scheme. The result is a very fast: 50K physical points, all directions of radiation and 680 frequencies require less than 5 minutes on an Apple M1 Laptop. The method is capable of handling variable absorption and scattering functions of spatial positions and frequencies.

The implementation is done using `htool`¹, a matrix compression library interfaced with the PDE solver `freefem++`. Applications to the temperature in the French Chamonix valley is presented at different hours of the day with and without snow / clouds and with a variable absorption taken from the Gemini measurements. The result is precise enough to assert temperature differences due to increased absorption in the vibrational frequency subrange of greenhouse gasses.

Keywords Radiative transfer, climatology, clouds, Integral equation, Navier-Stokes equation, H-matrix, Finite Element Methods.

Introduction

Heat transfer with radiative transfer are very important in astronomy, combustion and climatology, to name a few. For the atmosphere the reader is sent to [12],[9], [2], the numerically oriented book [17] and the two mathematically oriented books [4] and [5]. Due to the considerable difference of length scales, modelling at the level of photons is difficult to use for the earth atmosphere in large areas. A much simpler formulation, known as the radiative transfer equations, is based on energy conservation principles of continuum mechanics.

¹<https://github.com/htool-ddm/htool>

These were shown to be well posed in [15] for the Radiative Transfer system coupled with the time dependent heat equation. Existence and uniqueness was proved in [7] and [6] for the stationary case.

On the numerical side the problem is hard because the model has 3 space variables, two directional ones, the frequencies and time.

In 2005, K. Evans and A. Marshak wrote in chapter 4 of [12] a review of the numerical methods available for Radiative Transfer alone. Today, judging from [3], the situation has not changed: SHDOM (Spherical Harmonic Discrete Ordinate Method) and Monte-Carlo are the two most popular methods. While reviewing the current situation for the radiative transfer equations in [1] we implemented a finite element version of SHDOM and found that the method was incapable, unless a huge number of degree of freedom is used, of giving results with the accuracy needed to differentiate between small variations of the absorption coefficient.

One may resort to approximations. In nuclear physics and astronomy, for the numerical simulations in the 1960 a constant absorption coefficient was used, the so called Grey Model. In climatology, the grey model cannot explain the role of the greenhouse gasses.

The stratified approximation assumes that the surface which receives the radiations is flat and the source is far. Thus only one space variable is retained. For such cases, an integral formulation, probably due to Chandrasekhar [4], turns out to be much more precise and also computationally much cheaper. A fixed-point iteration scheme on this nonlinear integral formulation, known in the radiative transfer community as “iterations on the sources” was shown to be monotone in [14], a property which seems to have escaped earlier studies. Finally in [7], and [8] the method was extended to include the temperature equation of the fluid and also to handle Rayleigh scattering while retaining monotonicity. In [6] F. Golse observed that the integral formulation exists also in 3D. A new existence result was proved by using this formulation and it was numerically tested. However the computing cost was $O(N^2)$, N being the number of vertices of the triangulation of the physical domain.

The purpose of this article is to present an $O(N \ln N)$ implementation which uses compressed \mathcal{H} -matrices and views the computation of integrals as a matrix-vector product in the Finite Element discrete space. Thence P.H. Tournier, who is a co-author of the library `htool` for integral equations with \mathcal{H} -matrices, wrote the necessary modifications for Radiative Transfer, namely the handling of mixed matrices with one vertex on the boundary and the other one inside the domain.

The programming is a joint work of F. Hecht, O. Pironneau and P.H. Tournier, done using the high level PDE solver `freefem++` [10].

The method is tested on a 35×35 km area and the first 10km of the atmosphere above it. The center of the domain is the city of Chamonix in the French Alps, provided by D. Smets who has constructed high precision maps and an automatic triangular mesh generator for many places in the world for the Microsoft flight simulator. Hence this Radiative-Heat-Transfer code can be used easily for any other terrain. Note that such a study would be a challenge for Cartesian

meshes because some of the mountains like the Mont-Blanc are above 4000m and some slopes are almost vertical.

The absorption coefficient is a function of space and frequencies. It could also be a function of temperature if another fixed point loop is added. No regularity is assumed beside positivity and boundedness. Similarly, the scattering variable coefficient need only to be in $(0,1)$.

Real life data are used; the scattering part is not yet implemented As shown in [?], it is not so difficult to do, but it adds complexity to an already complex topic. Numerically, the methods is very fast: it can handle a few hundred thousand physical points plus all directions plus 680 frequency points on a PC (and a few millions on a supercomputer) within minutes.

Note that the authors have no competence for climate modelling, so the results are only briefly commented: the purpose of this study is to validate the numerical tool.

1 The Mathematical Problem

To find the temperature T in an incompressible fluid exposed to electromagnetic radiations, it is necessary to solve the Navier-Stokes equations coupled with the Radiative Transfer equations. It is a system of partial differential equations formulated in terms of the fluid velocity \mathbf{u} , its pressure p , its density ρ , and temperature T ; all are functions of time t and position \mathbf{x} in the physical domain Ω . It involves also the light intensity field $I_\nu(\mathbf{x}, t, \boldsymbol{\omega}, t)$ for each frequency ν in each direction $\boldsymbol{\omega}$:

Given $I_\nu, T, \mathbf{u}, \rho$ at $t = 0$, find $I_\nu, T, \mathbf{u}, \rho$, s.t. $\{\mathbf{x}, \boldsymbol{\omega}, t, \nu\} \in \Omega \times \mathbb{S}^2 \times (0, \bar{T}) \times \mathbb{R}^+$,

$$\begin{aligned} \frac{1}{c} \partial_t I_\nu + \boldsymbol{\omega} \cdot \nabla I_\nu + \rho \tilde{\kappa} a \left[I_\nu - \frac{1}{4\pi} \int_{\mathbb{S}^2} p_\nu(\boldsymbol{\omega}, \boldsymbol{\omega}') I_\nu(\boldsymbol{\omega}') d\boldsymbol{\omega}' \right] \\ = \rho \tilde{\kappa} (1 - a) [B_\nu(T) - I_\nu], \\ \rho (\partial_t T + \mathbf{u} \cdot \nabla T) - \nabla \cdot (\rho \kappa_T \nabla T) + A \nabla \cdot \int_0^\infty \frac{1}{4\pi} \int_{\mathbb{S}^2} I_\nu(\boldsymbol{\omega}) \boldsymbol{\omega} d\boldsymbol{\omega} d\nu = 0 \\ \partial_t \mathbf{u} + \mathbf{u} \cdot \nabla \mathbf{u} - \frac{\mu_F}{\rho} \Delta \mathbf{u} + \frac{1}{\rho} \nabla p = \mathbf{g}(T), \quad \nabla \cdot \mathbf{u} = 0, \quad \partial_t \rho + \nabla \cdot (\rho \mathbf{u}) = 0, \end{aligned} \quad (1)$$

where $A = 4\pi/c_P$, c_P is the specific heat of the medium at constant pressure, \mathbb{S}^2 is the unit sphere, ∇, Δ are with respect to \mathbf{x} , $B_\nu(T) = \frac{2\hbar\nu^3}{c^2 [e^{\frac{\hbar\nu}{kT}} - 1]}$, is the Planck function, \hbar, c, k are the Planck constant, the speed of light in the medium and the Boltzmann constant. The above holds only if c_P is constant in Ω , which is the case in moderate size domains.

1.1 Adimensionalization

Recall that $c = 2.99 \cdot 10^9 m \cdot s^{-1}$, $\hbar = 6.63 \cdot 10^{-34} J \cdot s$, $k = 1.38 \cdot 10^{-23} J \cdot K^{-1}$,

$\kappa_T = 2 \cdot 10^{-5} m^2 \cdot s^{-1}$, $c_P = 1.1 J \cdot s \cdot (g \cdot K)^{-1}$, $\rho \sim \bar{\rho} := 1.3g \cdot m^{-3}$, in air at 20°C.

The frequencies of interest are in the order of $\nu_0 = 10^{14} s^{-1}$, so we define $B_0 = \frac{2h\nu_0^3}{c^2}$, $T_0 = \frac{h\nu_0}{k}$ and work with I_ν/B_0 , T/T_0 and ν/ν_0 . Then (1) holds with these new unknowns with $B_\nu(T) = \nu^3/(e^{\frac{\nu}{T}} - 1)$, $c_P = 1$ and

$$B_0 = 1.47 \text{ J} \cdot \text{m}^{-2} \quad T_0 = 4789 \text{ K}, \quad \frac{A}{\bar{\rho}} = \frac{4\pi B_0 \nu_0}{c_P \bar{\rho} T_0} = 2.70 \cdot 10^{11} \text{ m} \cdot \text{s}^{-1}. \quad (2)$$

Notation 1 If $\bar{\rho}$ is a reference density for the gas, $\kappa := \bar{\rho} \tilde{\kappa}$ is the percentage of light absorbed per unit length. It has the dimension m^{-1} , thence, the notation

$$\kappa(\mathbf{x}, \nu) := \rho(\mathbf{x}) \tilde{\kappa}_\nu(\mathbf{x}).$$

Later we may assume at times that $\tilde{\kappa}_\nu(\mathbf{x})$ is independent of \mathbf{x} or is the sum of products of \mathbf{x} -functions with ν -functions.

The scattering albedo is $a \in (0, 1)$ and $\frac{1}{4\pi} p_\nu(\boldsymbol{\omega}, \boldsymbol{\omega}')$ is the ‘‘probability’’ that a ray in direction $\boldsymbol{\omega}'$ scatters in direction $\boldsymbol{\omega}$. Both κ and a are functions of ν . We further assume that $\nu \mapsto \kappa$ and $\nu \mapsto a$ are continuous positive functions, satisfying, for some positive constants a_M and $\kappa_m < \kappa_M$:

$$0 \leq \kappa_m \leq \kappa \leq \kappa_M, \quad 0 \leq a \leq a_M < 1, \quad \forall \nu > 0.$$

The viscosity of air μ_F is $18 \cdot 10^{-6} \text{ Pa}\cdot\text{s}$; $\mathbf{g}(T)$, the Boussinesq term, is a vector valued function of the temperature T .

We require Ω to be an open bounded subset of \mathbf{R}^3 with C^1 boundary. We denote by $\mathbf{n}(\mathbf{x})$ the outward unit normal to $\Gamma := \partial\Omega$ at \mathbf{x} .

Boundary conditions are needed, for example, initial values for $I_\nu, T, \mathbf{u}, \rho, \mathbf{u}$ given on Γ and ρ given at $\mathbf{x} \in \Gamma$ where $\mathbf{u} \cdot \mathbf{n} < 0$ and

$$I_\nu(\mathbf{x}, \boldsymbol{\omega}) = Q_\nu(\mathbf{x}, \boldsymbol{\omega}), \quad \boldsymbol{\omega} \cdot \mathbf{n} < 0, \quad \left. \frac{\partial T}{\partial n} \right|_\Gamma = 0.$$

1.1.1 Sunlight

When $Q_\nu(\mathbf{x}, \boldsymbol{\omega})$ is due to sunlight, of power Q^0 coming from the direction $\boldsymbol{\omega}_s$, then the surface which receives the light re-emits it with (Lambertian reflexion),

$$Q_\nu(\mathbf{x}, \boldsymbol{\omega}) = Q_\nu(\mathbf{x}) \cdot [\boldsymbol{\omega} \cdot \mathbf{n}(\mathbf{x})]_- \quad \text{with } Q_\nu(\mathbf{x}) := Q^0 [\boldsymbol{\omega}_s \cdot \mathbf{n}(\mathbf{x})]_+ B_\nu(T_s),$$

the Planck function with the Sun’s temperature T_s .

1.2 Simplifications

The angular average radiative intensity plays an important role in this article:

$$J_\nu(\mathbf{x}, t) = \frac{1}{4\pi} \int_{\mathbb{S}^2} I_\nu(\boldsymbol{\omega}) d\boldsymbol{\omega}.$$

Averaging the first equation in (1) and neglecting the time dependent term because $c \gg 1$, gives :

$$\nabla \cdot \int_0^\infty \int_{\mathbb{S}^2} I_\nu(\boldsymbol{\omega}) \boldsymbol{\omega} d\boldsymbol{\omega} d\nu = 4\pi \int_0^\infty \rho \tilde{\kappa}(1-a) (B_\nu(T) - J_\nu) d\nu, \quad (3)$$

which, in turn, leads to a simpler form (see (4)) for the second equation in (1).

1.2.1 Isotropic Scattering

Assume isotropic scattering: $p_\nu(\boldsymbol{\omega}, \boldsymbol{\omega}') \equiv 1$. Let us neglect the variations of ρ in the diffusion term of the temperature equation. Let us neglect $\frac{1}{c} \partial_t T$ because c is very large and let us assume that the Boussinesq term is small. Then the Navier-Stokes equations are decoupled and can be solved before hand. Then in the Radiative transfer and temperature equations ρ, \mathbf{u} are given. So (1) becomes the following system for I_ν, J_ν, T :

$$\begin{cases} \boldsymbol{\omega} \cdot \nabla I_\nu + \rho \tilde{\kappa} I_\nu = \rho \tilde{\kappa}(1-a) B_\nu(T) + \rho \tilde{\kappa} a J_\nu, & J_\nu := \frac{1}{4\pi} \int_{\mathbb{S}^2} I_\nu d\boldsymbol{\omega}, \\ \partial_t T + \mathbf{u} \cdot \nabla T - \nabla \cdot (\kappa_T \nabla T) = A \int_0^\infty \tilde{\kappa}(1-a) (J_\nu - B_\nu(T)) d\nu, & (4) \\ I_\nu(\mathbf{x}, \boldsymbol{\omega}) = Q_\nu(\mathbf{x}, \boldsymbol{\omega}), \quad \boldsymbol{\omega} \cdot \mathbf{n} < 0, \quad \mathbf{x} \in \partial\Omega, & \frac{\partial T}{\partial n} \Big|_{\partial\Omega} = 0, \quad T|_{t=0} = T_0. \end{cases}$$

1.2.2 Small Thermal Diffusion and Convection

When the convective velocity and κ_T are small compared to A , the temperature equation reaches a stationary states and simplifies to an integral relation between J and $B_\nu(T)$ and the system becomes:

$$\boldsymbol{\omega} \cdot \nabla I_\nu + \rho \tilde{\kappa} I_\nu = \rho \tilde{\kappa}(1-a) B_\nu(T) + \rho \tilde{\kappa} a J_\nu, \quad J_\nu := \frac{1}{4\pi} \int_{\mathbb{S}^2} I_\nu d\boldsymbol{\omega}, \quad (5)$$

$$\int_0^\infty \rho \tilde{\kappa}(1-a) (J_\nu - B_\nu(T)) d\nu = 0, \quad (6)$$

$$I_\nu(\mathbf{x}, \boldsymbol{\omega}) = Q_\nu(\mathbf{x}, \boldsymbol{\omega}) \text{ on } \Sigma := \{(\mathbf{x}, \boldsymbol{\omega}) \in \Gamma \times \mathbb{S}^2 : \boldsymbol{\omega}(\mathbf{x}) \cdot \mathbf{n}(\mathbf{x}) < 0\}. \quad (7)$$

The system is 6 dimensional in $[\mathbf{x} = [x, y, z], \boldsymbol{\omega} = [\omega_1, \omega_2, \omega_3 : |\boldsymbol{\omega}| = 1], \nu]$.

1.2.3 The stratified case

When Ω is thin in a direction Ox and the physical data depend mostly on x , the equations becomes almost one dimensional in x . The domain Ω is locally $(0, H) \times \mathbb{R}^2$. Assuming that sunlight at $x = +\infty$ crosses the atmosphere unaffected the equations reduce to

$$\begin{cases} \mu \partial_x I_\nu + \rho \tilde{\kappa} I_\nu = \rho \tilde{\kappa}(1-a) B_\nu(T) + \rho \tilde{\kappa} a J_\nu, & J_\nu := \frac{1}{2} \int_0^1 I_\nu d\mu \\ \int_0^\infty \rho \tilde{\kappa}(1-a) (J_\nu - B_\nu(T)) d\nu = 0, & (8) \\ I_\nu(0, \mu) = Q_\nu(\mathbf{x}, \mu), \quad \mu < 0, \quad I_\nu(H, \mu) = 0, \quad \mu > 0. \end{cases}$$

with Γ the plane $x = 0$, $Q_\nu = Q^0 B_\nu(T_s)\mu$, $\mu := \cos \alpha$ and α the angle of the ray $\boldsymbol{\omega}$ with Ox .

2 The Method of Characteristics

Let us derive a closed form solution of (5) by computing the long time solution of

$$\partial_\tau I(\mathbf{x}, \tau) + \boldsymbol{\omega} \nabla_{\mathbf{x}} I(\mathbf{x}, \tau) + \kappa(\mathbf{x}) I(\mathbf{x}, \tau) = S(\mathbf{x}). \quad (9)$$

While it plays no part, notice that $\tau = t/c$. Let $K(\mathbf{x}, \boldsymbol{\omega}, \tau) = \int_0^\tau \kappa(\mathbf{x} + \boldsymbol{\omega}s) ds$. Then

$$\frac{d}{d\tau} (I(\mathbf{x} + \boldsymbol{\omega}\tau, \tau) e^{K(\mathbf{x}, \boldsymbol{\omega}, \tau)}) = e^{K(\mathbf{x}, \boldsymbol{\omega}, \tau)} [\partial_\tau I + \boldsymbol{\omega} \nabla_{\mathbf{x}} I + \kappa(\mathbf{x}) I]_{|\mathbf{x} + \boldsymbol{\omega}\tau, \boldsymbol{\omega}, \tau}$$

Consequently

$$I(\mathbf{x} + \boldsymbol{\omega}\tau, \tau) e^{K(\mathbf{x}, \boldsymbol{\omega}, \tau)} = I(\mathbf{x}, 0) + \int_0^\tau e^{K(\mathbf{x}, \boldsymbol{\omega}, s)} S(\mathbf{x} + \boldsymbol{\omega}s) ds.$$

Denote $\mathbf{x}' = \mathbf{x} + \boldsymbol{\omega}\tau$; the above is also

$$I(\mathbf{x}', \tau) e^{K(\mathbf{x}' - \boldsymbol{\omega}\tau, \boldsymbol{\omega}, \tau)} = I(\mathbf{x}' - \boldsymbol{\omega}\tau, 0) + \int_0^\tau e^{K(\mathbf{x}' - \boldsymbol{\omega}\tau, \boldsymbol{\omega}, s)} S(\mathbf{x} + \boldsymbol{\omega}s) ds.$$

Denote by $\tau_{\mathbf{x}', \boldsymbol{\omega}}$ the value of τ which brings $\mathbf{x}' - \boldsymbol{\omega}\tau$ to the boundary:

$$\mathbf{x}' - \boldsymbol{\omega}\tau_{\mathbf{x}', \boldsymbol{\omega}} \in \Sigma, \text{ and denote } \mathbf{x}_\Sigma(\mathbf{x}', \boldsymbol{\omega}) := \mathbf{x}' - \boldsymbol{\omega}\tau_{\mathbf{x}', \boldsymbol{\omega}}.$$

Then the long time solution of (9) is

$$\begin{aligned} I(\mathbf{x}') &= I(\mathbf{x}_\Sigma(\mathbf{x}', \boldsymbol{\omega})) e^{-K(\mathbf{x}_\Sigma(\mathbf{x}', \boldsymbol{\omega}), \boldsymbol{\omega}, \tau)} \\ &\quad + \int_0^{\tau_{\mathbf{x}', \boldsymbol{\omega}}} e^{K(\mathbf{x}' - \boldsymbol{\omega}s, \boldsymbol{\omega}, s) - K(\mathbf{x}_\Sigma(\mathbf{x}', \boldsymbol{\omega}), \boldsymbol{\omega}, \tau_{\mathbf{x}', \boldsymbol{\omega}})} S(\mathbf{x}' - \boldsymbol{\omega}(\tau_{\mathbf{x}', \boldsymbol{\omega}} - s)) ds. \end{aligned}$$

It can also be written as:

$$\begin{aligned} I(\mathbf{x}, \boldsymbol{\omega}) &= I(\mathbf{x}_\Sigma(\mathbf{x}, \boldsymbol{\omega})) e^{-\int_0^{\tau_{\mathbf{x}, \boldsymbol{\omega}}} \kappa(\mathbf{x} - \boldsymbol{\omega}s) ds} + \int_0^{\tau_{\mathbf{x}, \boldsymbol{\omega}}} e^{-\int_0^s \kappa(\mathbf{x} - \boldsymbol{\omega}s') ds'} S(\mathbf{x} - \boldsymbol{\omega}s) ds \\ &= I(\mathbf{x}_\Sigma(\mathbf{x}, \boldsymbol{\omega})) e^{-\int_{[\mathbf{x}, \mathbf{x}_\Sigma]} \kappa} + \int_{[\mathbf{x}, \mathbf{x}_\Sigma]} e^{-\int_{[\mathbf{x}, \mathbf{x}']} \kappa} S(\mathbf{x}') dx'. \end{aligned} \quad (10)$$

Averaging in $\boldsymbol{\omega}$ and using (7), and knowing that the solid angle integral of $f(x - \boldsymbol{\omega}s) d\boldsymbol{\omega}$ is the surface integral on Γ of $f(\mathbf{x}' - \mathbf{x}) \cdot \mathbf{n}(\mathbf{x}') |\mathbf{x}' - \mathbf{x}|^{-3} d\Gamma(x')$ leads to :

$$\begin{aligned} J_\nu(\mathbf{x}) &:= \frac{1}{4\pi} \int_{\mathbb{S}^2} I(\mathbf{x}, \boldsymbol{\omega}) d\boldsymbol{\omega} = \frac{1}{4\pi} \int_{\mathbb{S}^2} I(\mathbf{x}_\Sigma(\mathbf{x}, \boldsymbol{\omega})) e^{-\int_0^{\tau_{\mathbf{x}, \boldsymbol{\omega}}} \kappa(\mathbf{x} - \boldsymbol{\omega}s) ds} d\boldsymbol{\omega} \\ &\quad + \frac{1}{4\pi} \int_{\mathbb{S}^2} \int_0^{\tau_{\mathbf{x}, \boldsymbol{\omega}}} e^{-\int_0^s \kappa(\mathbf{x} - \boldsymbol{\omega}s') ds'} S(\mathbf{x} - \boldsymbol{\omega}s) ds d\boldsymbol{\omega} \\ &= S_\nu^E(\mathbf{x}) + \mathcal{J}[S](\mathbf{x}). \end{aligned} \quad (11)$$

with the notations, $z_- := -\min(z, 0)$ and

$$S_\nu^E(\mathbf{x}) := \frac{1}{4\pi} \int_\Gamma Q_\nu(\mathbf{x}, \frac{\mathbf{x}' - \mathbf{x}}{|\mathbf{x}' - \mathbf{x}|}) \frac{[(\mathbf{x}' - \mathbf{x}) \cdot \mathbf{n}(\mathbf{x}')]_-}{|\mathbf{x}' - \mathbf{x}|^3} e^{-\int_{[\mathbf{x}, \mathbf{x}']} \kappa} d\Gamma(\mathbf{x}') \quad (12)$$

$$\mathcal{J}[S](\mathbf{x}) := \frac{1}{4\pi} \int_\Omega S(\mathbf{x}') \frac{e^{-\int_{[\mathbf{x}, \mathbf{x}']} \kappa}}{|\mathbf{x}' - \mathbf{x}|^2} dx'.$$

where $\mathbf{n}(\mathbf{x}')$ is the outer normal at $\mathbf{x}' \in \partial\Omega$. The last line is true only if Ω is convex but it can be used in the general case with the following definition of $\bar{\Omega}$ and $\bar{\kappa}$.

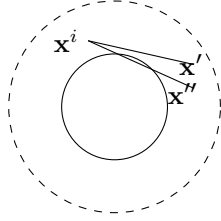


Figure 1: Consider Ω , the domain between the 2 spheres. The segment $[\mathbf{x}^i, \mathbf{x}']$ participates to the radiative intensity in \mathbf{x}^i . However when the segment $[\mathbf{x}^i, \mathbf{x}'']$ crosses the inner sphere, the light scattered from \mathbf{x}'' does not contribute to the light intensity in \mathbf{x}^i .

Proposition 1 *Let $\bar{\Omega} \supset \Omega$ be a convex extension of Ω . Let $\bar{\kappa}$ be an extension of κ in $\bar{\Omega}$ such that*

$$\bar{\kappa}(\mathbf{x}) = \kappa(v\mathbf{x}), \quad \mathbf{x} \in \Omega, \quad \bar{\kappa}(\mathbf{x}) = +\infty, \quad \mathbf{x} \in \bar{\Omega} \setminus \Omega.$$

Then

$$\int_{\mathbb{S}^2} \int_0^{\tau_{\mathbf{x}, \boldsymbol{\omega}}} e^{-\int_0^s \kappa(\mathbf{x} - \boldsymbol{\omega} s') ds'} S(\mathbf{x} - \boldsymbol{\omega} s) ds d\boldsymbol{\omega} = \int_{\bar{\Omega}} S(\mathbf{x}') \frac{e^{-\int_{[\mathbf{x}, \mathbf{x}']} \bar{\kappa}}}{|\mathbf{x} - \mathbf{x}'|^2} dx'.$$

Proof: If Ω is convex then $\{\mathbf{x} - \boldsymbol{\omega} s : s \in (0, \tau_{\mathbf{x}, \boldsymbol{\omega}}), \boldsymbol{\omega} \in \mathbb{S}^2\} = \Omega$. Referring to figure 1, if Ω is not convex, then the part in $\bar{\Omega} \setminus \Omega$ of the integral on the right is zero because $\mathbf{x}' \in \bar{\Omega} \setminus \Omega$ implies that a portion of the integral in the exponential will be on $[\mathbf{x}'', \mathbf{x}']$, for some $\mathbf{x}'' \in \bar{\Omega} \setminus \Omega$. This portion will contribute to the integral with $\bar{\kappa} = +\infty$ and $e^{-\infty} = 0$. \square

2.0.1 The Stratified Grey Case

The following will be helpful to assert the precision of the general algorithm 2.1 below.

Recall the Stefan-Blotzmann relation: $\int_0^\infty B_\nu(T) = \sigma T^4$ with $\sigma = \pi^4/15$, the Stefan constant. If $\tilde{\kappa}_\nu$ is constant (grey case), then (8) integrated in ν yields an equation for $\bar{I} = \int_0^\infty I_\nu d\nu$:

$$\mu \partial_x \bar{I} + \rho \tilde{\kappa} \bar{I} = \rho \tilde{\kappa} \sigma T^4(x), \quad \sigma T^4(x) = \frac{1}{2} \int_{-1}^1 \bar{I}(x, \mu) d\mu, \quad x \in (0, H) \quad (13)$$

with boundary conditions $\bar{I}(0, \mu)|_{\mu>0} = \mu Q^0 \sigma T_s^4$ and $\bar{I}(H, \mu)|_{\mu<0} = 0$. Even though one can find directly a solution in integral form, when $\rho \tilde{\kappa}$ is constant the above framework yields

$$\bar{S}^E(\mathbf{x}) = \frac{Q^0 \sigma T_s^4}{4\pi} \int_{\mathbb{R}^2} \left(\frac{\cos^2 \theta}{x} \right)^2 e^{-\frac{\kappa x}{\cos \theta}} d\Gamma(y, z) = \frac{Q^0 \sigma T_s^4}{2} \mathbf{E}_3(\kappa x) \quad (14)$$

where \mathbf{E}_3 is the third exponential integral. Similarly (see [8])

$$\mathcal{J}[S](x) = \kappa \int_0^H S(x') \mathbf{E}_1(\kappa|x' - x|) dx'. \quad (15)$$

This approximation can be extended to the case κ function of x by a change of coordinate $x \rightarrow \tau$ with $\kappa \frac{\partial}{\partial \tau} = \frac{\partial}{\partial x}$.

2.1 Algorithm

System (4) can be solved by the following iterative scheme.

1. Start from $T^0 \equiv 0$ and $J_\nu^0 = S_\nu^E$, given by (12)

2. FOR $n = 0, 1, \dots, N - 1$

(a) Knowing $T^n(\mathbf{x}, t)$ and $J_\nu^n(\mathbf{x}, t)$, compute by (11)

$$J_\nu^{n+1} = S_\nu^E + \mathcal{J}[a J_\nu^n + (1 - a) B_\nu(T^n)], \quad \nu \in (0, \infty), \quad \mathbf{x} \in \Omega, \quad t < T.$$

(b) Define T^{n+1} the solution of the semilinear drift-diffusion equation

$$\begin{cases} \rho c_V (\partial_t T^{n+1} + \mathbf{u} \cdot \nabla_x T^{n+1}) - \nabla_x \cdot (\rho c_P \kappa_T \nabla_x T^{n+1}) \\ \quad + \mathcal{B}(T^{n+1}) = 4\pi \int_0^\infty \kappa(1 - a) J_\nu^{n+1} d\nu, \\ T^{n+1}|_{t=0} = T_0, \quad \frac{\partial T^{n+1}}{\partial n} \Big|_{\partial \Omega} = 0, \quad \mathbf{x} \in \Omega, \quad t > 0, \end{cases}$$

where ρ and \mathbf{u} are given by the Navier-Stokes equations and

$$\mathcal{B}(T) := 4\pi \int_0^\infty \kappa(1 - a) B_\nu(\min(T_+, T_M)) d\nu.$$

Remark 1 When \mathbf{u} and κ_T are negligible, Step (b) becomes: find T^{n+1} such that

$$\int_0^\infty \kappa(1 - a) B_\nu(T_+^{n+1}) d\nu = \int_0^\infty \kappa(1 - a) J_\nu^{n+1} d\nu. \quad (16)$$

This equation has a unique solution because $T \mapsto B_\nu(T)$ is increasing. As for existence, observe that the left hand-side is continuous in T_+ , vanishes for $T_+ = 0$, and tends to $+\infty$ when $T_+ \rightarrow +\infty$. For a computer solution we may use a Newton method because the Hessian is positive and never vanishes.

3 Implementation with \mathcal{H} -Matrices

Note that the computations of S_ν^E and $\mathcal{J}[S]$ involve convolution like operators. Indeed, with Ω convex bounded and $a = 0$, S^E is given by (12) and

$$\mathcal{J}[S_\nu](\mathbf{x}) = \frac{1}{4\pi} \int_{\Omega} S_\nu(\mathbf{x}') \kappa(\mathbf{x}') \frac{e^{-\int_{[\mathbf{x}, \mathbf{x}']} \kappa}}{|\mathbf{x} - \mathbf{x}'|^2} dx'. \quad (17)$$

The domain is discretized by the vertices $\{\mathbf{x}^i\}_1^N$ of a tetraedral mesh. The integrals are computed with a quadrature rule using quadrature points inside the tetraedras, typically 25 points when \mathbf{x}^i is near to the tetraedra of the integral and 5 points otherwise ; J is approximated by its P^1 interpolation on the mesh:

$$J(\mathbf{x}) = \sum_1^N J_j \hat{w}^j(\mathbf{x}) \quad \text{where } \hat{w}^j \text{ is the } P^1\text{- Finite Element hat function of vertex } \mathbf{x}^j.$$

Then Step (a) of Algorithm 2.1 becomes:

$$\begin{aligned} S_{\nu,j} &= aJ_{\nu,j} + (1-a)B_\nu(T_j) \\ J_{\nu,i} &= S_{\nu,i}^E + \sum_j G_\kappa^{ij} S_{\nu,j} \quad \text{where } G_\kappa^{ij} = \frac{1}{4\pi} \int_{\Omega} \kappa \frac{e^{-\int_{[\mathbf{x}^i, \mathbf{x}']} \kappa}}{|\mathbf{x}^i - \mathbf{x}'|^2} \hat{w}^j(\mathbf{x}') dx' \end{aligned} \quad (18)$$

The matrix \mathbf{G} can be compressed with the \mathcal{H} -matrix method so that the multiplication $\mathbf{G} \cdot \mathbf{S}$ has complexity $O(N \ln N)$ for each ν . The method works best when the kernel of G in the integral decays exponentially with the distance between \mathbf{x}^i and \mathbf{x}' . The \mathcal{H} -matrix approximation views $\{G^{ij}\}$ as a hierarchical tree of square blocks; The blocks correspond to interaction between clusters of points near \mathbf{x}^j and near \mathbf{x}' . Far-field interaction blocks can be approximated by a low rank matrix because their singular value decompositions (SVD) have fast decaying singular values. We use *partially pivoted adaptive cross-approximation* [16] to approach the first terms of the SVD of the blocks, because only r -rows times r -columns columns are needed instead of the whole block, where r is the rank of the approximation. The rank is a function of a user defined parameter ϵ in connection with the relative Frobenius norm error. Another criteria must be met: if R_1 (resp R_2) is the radius of a cluster of points centered at \mathbf{x}_1 (resp \mathbf{x}_2), then one goes down the hierarchical tree until the corresponding block satisfies $\max(R_1, R_2) < \eta |\mathbf{x}_1 - \mathbf{x}_2|$ where η is a user defined parameter. If the en of the tree is reached, the bloc is not compacted and it is displayed in red on figure 10. Then, to compute the integral $\int_0^\infty \kappa J_{\nu,i} d\nu$ a rectangular quadrature at points ν_k is used.

For example when $a = 0$,

$$\int_0^\infty \kappa J_{\nu,i} d\nu \approx \sum_k S_{\nu_k,i}^E (\nu_k - \nu_{k-1}) + \sum_k \sum_j \kappa_{\nu_k} G_{\kappa_{\nu_k}}^{ij} B_{\nu_k}(T_j) (\nu_k - \nu_{k-1}) \quad (19)$$

The same decomposition into product of \mathcal{H} -matrices with vectors $\{Q_{\nu_k}(\mathbf{x}^i)\}_{i=1}^N$ can be applied to compute $S_{\nu_k}^E$:

$$S_{\nu_k,i}^E = \sum_1^N S_{\kappa_{\nu_k}}^{ij} Q_{\nu_k}(\mathbf{x}^j), \quad S_{\kappa}^{ij} = \int_\Gamma \hat{w}^j e^{-\int_{[\mathbf{x}^i, \mathbf{x}^j]} \kappa} \left(\frac{[(\mathbf{x}' - \mathbf{x}^i) \cdot \mathbf{n}(x')]^+}{|\mathbf{x}' - \mathbf{x}^i|^2} \right)^2 ds(x') \quad (20)$$

3.1 Lebesgue Integrals

We will use the Gemini measurements to define κ_ν (figure 2). To represent such a function we require 683 ν -points. As it is, the numerical method requires an \mathcal{H} -matrix for each ν , but it is not feasible to define 2×683 \mathcal{H} -matrices!

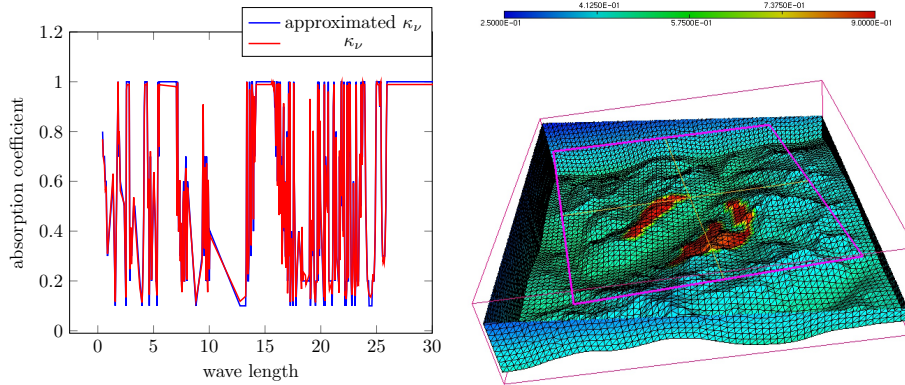


Figure 2: Absorption κ_ν versus wavelength (c/ν) in the range (0.1, 26) read from the Gemini data site[11]. In the \mathcal{H} -step of the algorithm it is approximated by $0.01 + \text{round}(10\kappa)/10$, shown here as “approximated κ_ν ”. Right: the x-dependency of κ , the topography and the mesh. The Mont-Blanc is in the bottom left part and Chamonix is in the center. Colors are levels of the x dependence of κ , $0.5(1 - x/2)$; the red part is the intersection of the cloud with the mountains; the cloud is a cylinder circumscribing the red parts, centered at Chamonix and between altitude 2000m and 8000m; it is used only in one simulation.

Observe that the \mathcal{H} -matrices \mathcal{H}, H^E , depend on ν directly but through κ_ν . It is an opportunity to reduce the number of \mathcal{H} -matrices down to the number of different values of κ_ν . The the integrals with respect to ν are evaluated much like a Lebesgue integral.

Suppose κ takes only 2 values κ_1 and κ_2 , then, according to (20), only 2 functions S_ν^E are need, S_1^E, S_2^E , and similarly for G_κ . Now (19) becomes

$$\begin{aligned} H_1^n &= \sum_{\{k:\kappa_{\nu_k}=\kappa_1\}} \kappa_1(\nu_k - \nu_{k-1}) \sum_j G_{\kappa_1}^{ij} B_{\nu_k}(T_j^n) \\ H_2^n &= \sum_{\{k:\kappa_{\nu_k}=\kappa_2\}} \kappa_2(\nu_k - \nu_{k-1}) \sum_j G_{\kappa_2}^{ij} B_{\nu_k}(T_j^n) \\ \int_0^\infty \kappa J_{\nu,i}^{n+1} &= s_1 \kappa_1 S_1^E + s_2 \kappa_2 S_2^E + H_1^n + H_2^n \end{aligned} \quad (21)$$

where s_j is the measure of the ν -set where $\kappa_\nu = \kappa_j$, $j = 1, 2$.

There are some limitations however: $\kappa(\mathbf{x})$ must be a sum of products of \mathbf{x} -functions by ν - functions:

$$\kappa_\nu(x) = \sum_j \rho_j(\mathbf{x}) \kappa_\nu^j, \text{ where } \kappa_\nu^j \text{ takes only } N_k^j \text{ different values } \{\kappa_k^j\}_k \quad (22)$$

Let $s_k^j := \{\nu : \kappa_\nu^j = \kappa_k^j\}$.. Then

$$\begin{aligned} \int_0^\infty \kappa_\nu(\mathbf{x}) \mathcal{J}[S(\nu, \mathbf{x})] d\nu &= \\ \frac{1}{4\pi} \sum_{i,j,l,k} \rho_j(\mathbf{x}) \kappa_k^j \kappa_l^i \int_\Omega \left[\int_{s_k^i} S(\nu, \mathbf{x}') d\nu \right] \rho_i(\cdot) \frac{e^{-\kappa_l^i \int_{[\mathbf{x}, \mathbf{x}']} \rho_i(\cdot)}}{|\mathbf{x} - \mathbf{x}'|^2} dx'. \end{aligned} \quad (23)$$

Hence only the \mathcal{H} -matrices of kernel $\rho_i(\mathbf{x}') \kappa_l^i \exp(-\kappa_l^i \int_{[\mathbf{x}, \mathbf{x}']} \rho_i(\cdot)) / |\mathbf{x} - \mathbf{x}'|^2$ are needed.

The same decomposition holds for S_ν^E .

$$\begin{aligned} \int_0^\infty \kappa_\nu(\mathbf{x}) S_\nu^E(\mathbf{x}) d\nu &= \\ \frac{1}{4\pi} \sum_{i,j,k,l} \rho_i(\mathbf{x}) \kappa_l^i \int_{\partial\Omega} \left[\int_{s_k^j} Q_\nu d\nu \right] e^{-\kappa_k^j \int_{[\mathbf{x}, \mathbf{x}']} \rho(\cdot)} \left(\frac{[(\mathbf{x}' - \mathbf{x}) \cdot \mathbf{n}(x')]^+}{|\mathbf{x}' - \mathbf{x}|^2} \right)^2 d\Gamma(x'), \end{aligned}$$

which, after discretization, involves only the sum of products of \mathcal{H} -matrices of kernel on $\partial\Omega$: $e^{-\kappa_k^j \int_{[\mathbf{x}, \mathbf{x}']} \rho_j(\cdot)} ([(\mathbf{x}' - \mathbf{x}) \cdot \mathbf{n}(x')]_-)^2 / |\mathbf{x}' - \mathbf{x}|^4$.

3.2 Computations of Exponentials on a Background Grid

To compute $e^{-\kappa_k^j \int_{[\mathbf{x}, \mathbf{x}']} \rho_j(\cdot)}$ we use a quadrature rule for the integral:

$$\int_{[\mathbf{x}, \mathbf{x}']} \rho_j(\cdot) \approx \sum_{i=0}^I \rho_j(\mathbf{x}_i) |\mathbf{x}_{i+1} - \mathbf{x}_i|, \quad \mathbf{x}_0 = \mathbf{x}, \quad \mathbf{x}_{I+1} = \mathbf{x}'.$$

To speed-up the computation of $\rho(\mathbf{x}_i)$, ρ is interpolated on a fine 3D Cartesian grid during the initialization phase of the computer program.

4 Validation

4.1 Computing Resources

To assert the precision and computing time we used several meshes. The grey case corresponds to $\kappa = 0.5(1 - x/2)$. The Gemini case is when $\kappa_\nu = (1 - x/2)\tilde{\kappa}_\nu$ with $\tilde{\kappa}_\nu$ read from the Gemini web site. Results are on table 1 for the Chamonix valley and on figure 6 for the flat ground case.

Table 1: Computing Times in seconds (Apple M1 8 proc)

nb vertices	4053	30855	231 796
Grey	3	19	170
Gemini	36	239	2027

The code has been ported on a supercomputer. It scales perfectly for the grey case and takes 90" for 300K vertices. On the Gemini case the Newton iterations are not yet parallelized but the rest takes 360". The memory used is governed by the compressed matrices. For the \mathcal{H} -matrices the compression ratio is 29 for the volumic kernel and 9 for the surfacic kernel.

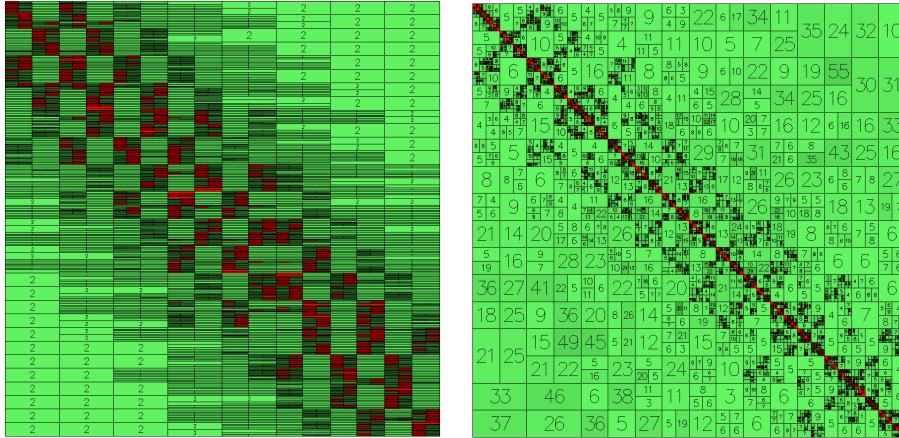


Figure 3: Compressed blocks in the \mathcal{H} -matrices, surfacic on the left, volumic on the right. Compression is shown by colors (lighter is more compressed, red is not compressed), numbers are the ranks of the approximations. Neighboring blocks may not have similar ranks because they maybe correspond to vertices far from each other in the physical space.

4.2 Length Scale, Values for κ_ν

The Gemini measurements for κ are used in a domain $\Omega = \mathbf{x} \in (0, 1) \times (-0.2, 3.32) \times (-3.35, 0.16)$ in 10km units. The Nimbus-4 measurements [13] show that some infra-red radiations like $\nu_{12} = \frac{3}{12} \cdot 10^{14} s^{-1}$, cross the 12km thick earth atmosphere almost unaffected, which implies that $\kappa_{\nu_{12}} \sim 0$.

Other radiations like $\nu_{15} = 0.2 \cdot 10^{14} s^{-1}$ are damped by 28% (i.e. $I_{\nu_{15}}|_{x=1} = 0.28 I_{\nu_{15}}|_{x=0}$, see [13]) which implies $e^{-1.2\kappa_{\nu_{15}}} = 0.28$, i.e. $\kappa_{\nu_{15}} = 1.05$. This is associated with the presence of CO_2 in air.

Similarly, corresponding to the presence of water in air, $I_{\nu_{20}}$ is damped by 20%, meaning that $\kappa_{\nu_{20}} \sim 0.3$.

Therefore the Gemini data can be used without scaling. For a grey model, $\kappa = 0.5$ corresponds to the average loss from the theoretical black body radiation at ground level to the actual measurements in space. Surely this value is too large in the visible range, but the correlation between the infra-red and the visible ranges is weak.

4.3 Temperatures on a Flat Land Exposed to Sunrays

Our purpose here is to validate the results against the stratified numerical solutions of [8]. We begin with a grey case, $\kappa = 0.5$. The domain is $\Omega = (0, 1 \times (-L, L) \times (-L, L)$ above the Earth surface $S: x = 0$. The radiations of the Sun cross the atmosphere unaffected; 30% is reflected and 70% is absorbed and then re-emitted as a black body in all directions (Lambertian reflection) with intensity given by (24). Since the downward travel of the radiations is ignored, the source of light is at $x = 0$, with

$$Q_\nu(\mathbf{x}, \boldsymbol{\omega}) = Q^0 B_\nu(T_s) \mathbf{n} \cdot \boldsymbol{\omega}, \quad Q^0 = 2 \cdot 10^{-5}, \quad T_s = 1.02, \quad \mathbf{n} = (1, 0, 0)^T \quad (24)$$

The results depend on the mesh size h and L . By increasing L and the number of vertices n^3 , convergence to the stratified case is reached (figure 4). The convergence rate is shown on figure 7 to be approximately $h^{1.5}$. The stratified solution is computed independently by a method sketched in Paragraph 2.0.1 and detailed in [?].

The CPU times are plotted on figure 6 for 5 meshes with $N = 616, 4056, 30855, 80898, 231796$ vertices respectively. It confirms the $N \log N$ growth.

A similar exercise is done with $\kappa_\nu = 0.5(1 - x/2)$. Comparison with the stratified case is possible after a change of variable in the stratified code. Results are shown on figure 5.

4.4 The Chamonix Valley: the Grey Case

The domain is a portion of the atmosphere $\Omega = [h(y, z), H] \times [y_m, y_M][z_m, z_M]$ above the Earth surface $S: x = h(y, z)$. The radiations of the Sun cross the atmosphere unaffected; 30% is reflected and 70% is absorbed and re-emitted

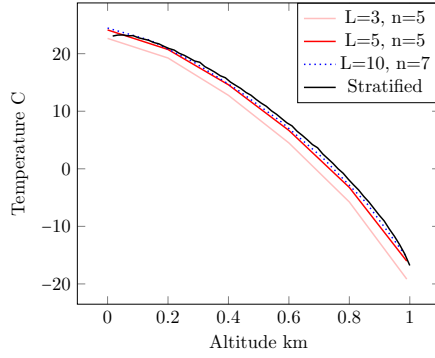


Figure 4: Temperatures $T(x, 0, 0)$ versus altitude x when $\kappa_\nu = \frac{1}{2}$ for some values of L and n . Convergence to the stratified 1D solution is visible.

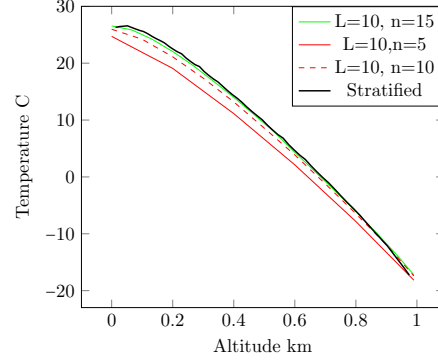


Figure 5: Temperatures when $\rho\tilde{\kappa} = \frac{1}{2}(1 - 0.5x)$: comparison with the stratified solution.

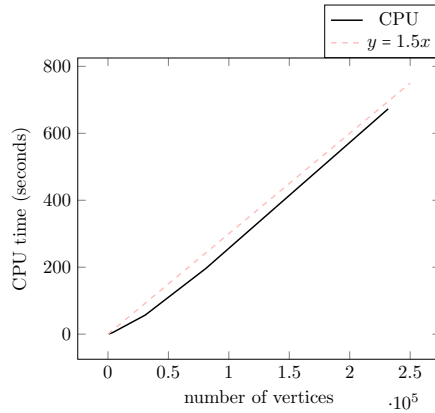


Figure 6: CPU time to compute the grey case on a flat ground, indicating an $N \ln N$ growth where N is the number of vertices in the mesh.

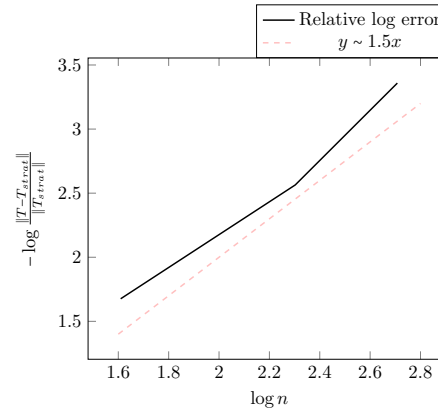


Figure 7: Log-log plot of the discretization error versus mesh size; the “exact” solution is the stratified one computed with many points.

with intensity (24), except that \mathbf{n} is the normal of S . We can account for the hour of the day by rotating accordingly all normals.

$$Q_\nu([h(y, z), y, z]^T, \boldsymbol{\omega}) = Q_0(\mathbf{x})B_\nu(T_s)\mathbf{n} \cdot \boldsymbol{\omega}, \quad T_s = 1.02,$$

We have simulated the case $Q_0 = 2 \cdot 10^{-5}$ (no snow) and the case with snow above 2500m:

$$Q_0(\mathbf{x}) = 0.5(\beta + (1 - \beta)\mathbf{1}_{x < h_{snow}}), \quad \beta = 0.3, \quad h_{snow} = 0.25, \quad \mathbf{x} \in S.$$

It means that in case of snow the light source is 30% of what it is without snow, the rest was reflected in the visible range before re-emission. Note that glaciers below 2500m are ignored.

As above we begin with a $\kappa_\nu = 0.5(1 - x/2)$ which takes into account the rarefaction of air. The mesh is shown on figure 8.

Temperatures and radiations are computed in the morning and evening when the sun is at $\pm 45^\circ$ from the vertical and inclined towards the South by 20° . Results are shown on figure 8. On all such figures the altitude has been multiplied by 2 to enhance the graphics. It can be seen that the temperature is high on the slopes exposed to the Sun. It is seen also that the temperature is much cooler where there is snow. Temperatures are clearly too low on high mountains and perhaps too hot also on sunlit slopes. Still it is reasonable for a grey model. The Mont-Blanc is on the top left. Recall that points near the border of the domain receive only half the light because of clipping, so it is unrealistically cooler near the border.

To check convergence we compared a lower solution with a higher one. To generate a lower solution initial reduced temperature in the algorithm was set to 0.01. To generate an upper solution, T^0 was set to 0.12. Instead of 7 iterations, 15 were needed to reduce $|T^{n+1} - T^n|$ below 10^{-11} . Then, no visible difference could be seen between the two results.

4.4.1 Influence of the snow

The snow is very important for the temperature distribution at the ground level. When there is no snow temperatures at the ground level in the Chamonix region at noon is $2^\circ C$ hotter in the valley and very much hotter in the mountain, above zero (figure 9).

4.4.2 Clouds

Let the cloud be a cylinder centered in the middle of the domain, between $x = 2000\text{m}$ and $x = 8000\text{m}$. There, $\kappa_\nu(\mathbf{x})$ is multiplied by 1.5:

$$\kappa_\nu = 0.5(1 - 0.5x)(1 + 0.5\mathbf{1}[x \in (0.2, 0.8) : (y - 1.5)^2 + (z + 1.5)^2 < 0.5]);$$

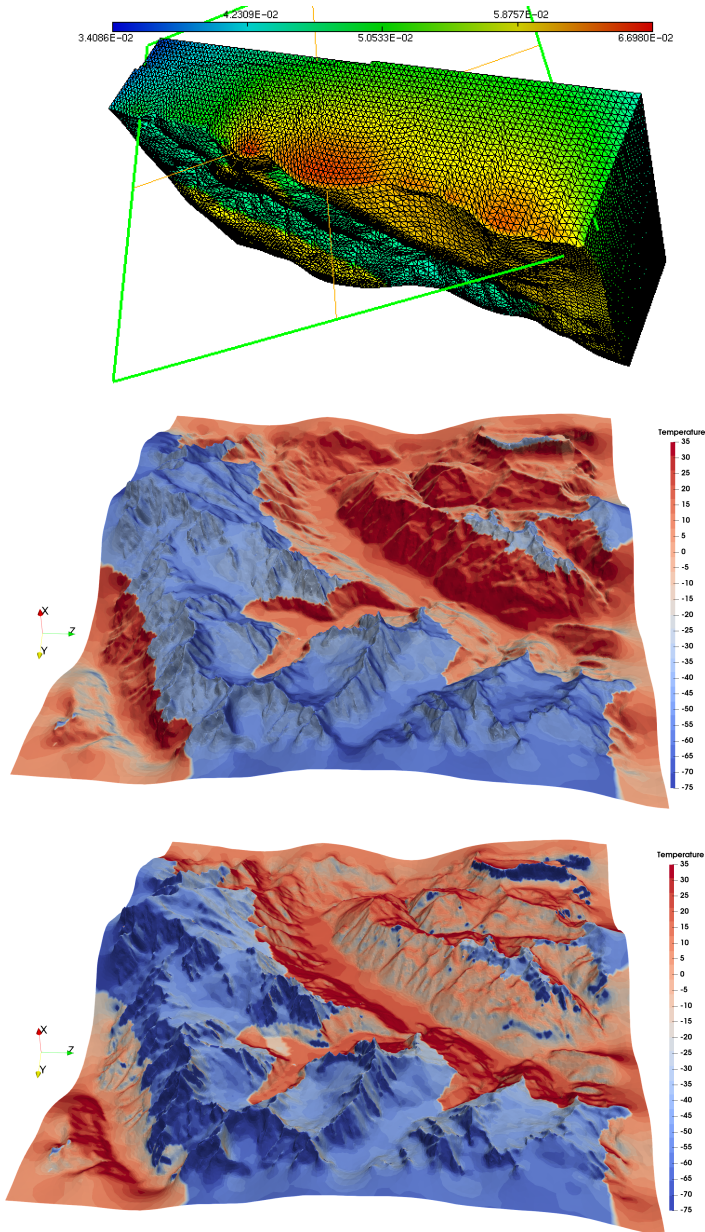


Figure 8: All 3 computations are with $\kappa_\nu = 0.5(1 - x/2)$ and a clear sky (no cloud). Top: Reduced temperatures at noon in a vertical cut of the domain (the mesh has 36K vertices). Middle: Ground level temperatures in the morning: the Sun is at 45° from vertical in (x,y) plane and -20° in the (x,z) plane. (Est is the lower side of the square, South is the left side). Bottom: Temperatures in the evening ((sun at -45° from vertical in (x,y) plane and -20° in the (x,z) plane; West is the upper side of the square). Both meshes have 360K vertices.

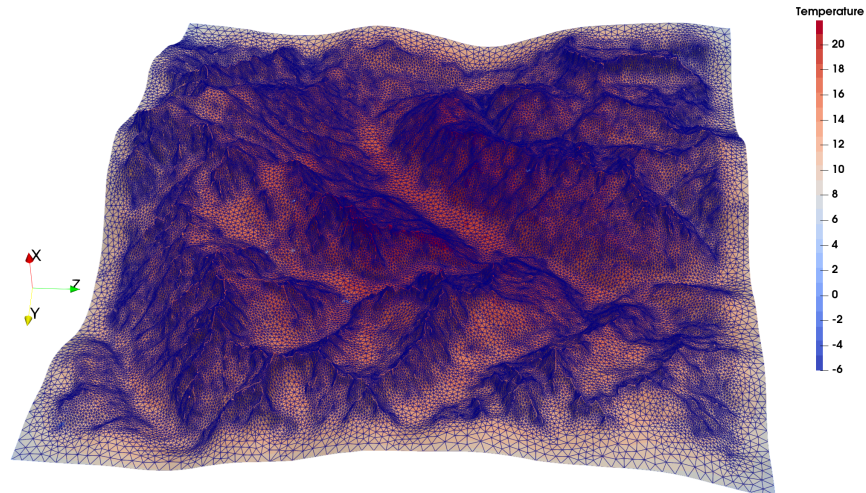
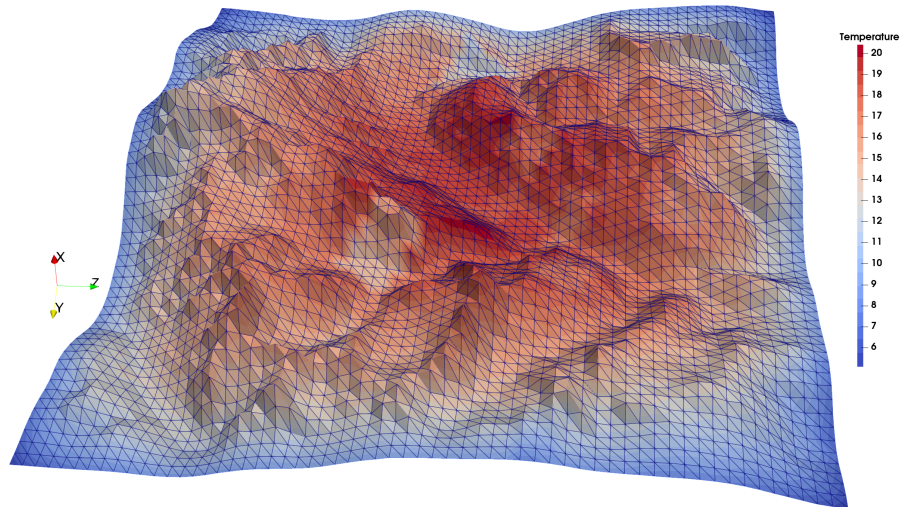


Figure 9: Influence of the snow and the mesh: Ground temperatures at noon without snow. It is 2°C hotter in the valley and very much hotter in the mountain, naturally. On top, the mesh has 36K vertices, and below, it has ten times more vertices. the two pictures differ mostly near the border of the domain where the computations are wrong anyway because the points receive only one half of the sunshine other points receive (and one fourth at the corners).

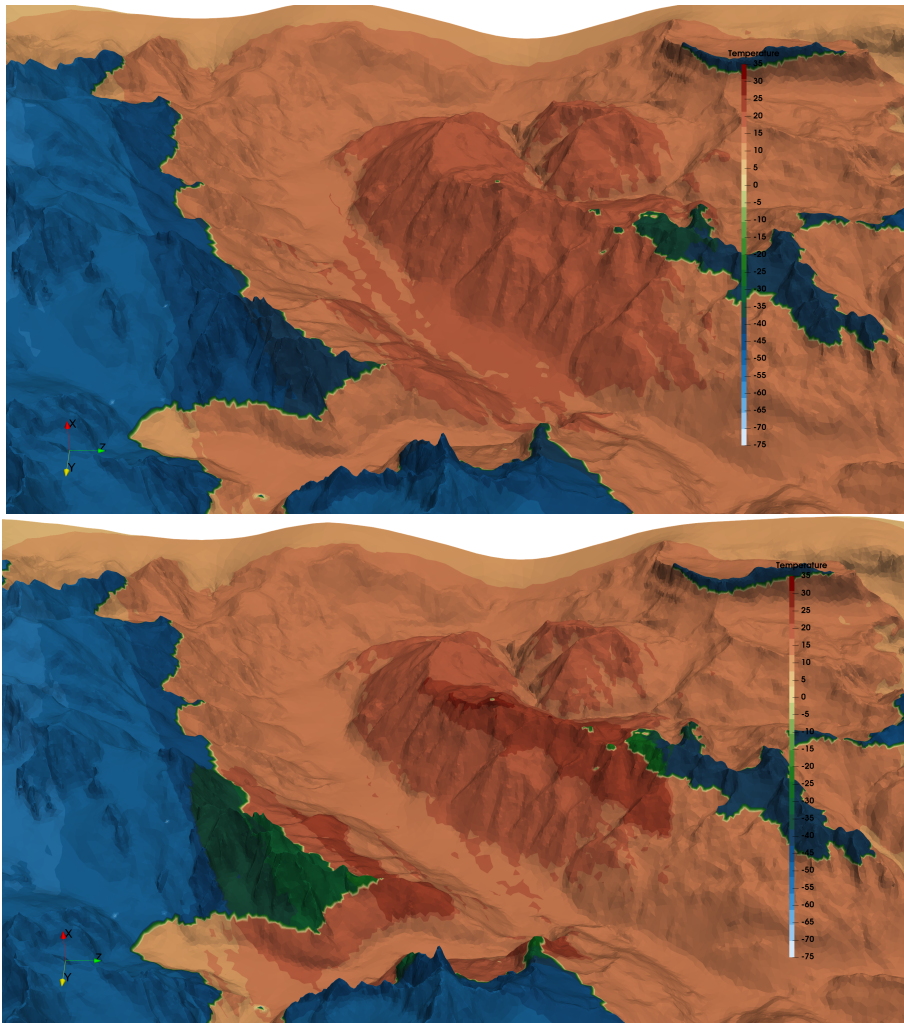


Figure 10: Ground temperature in the Chamonix region at noon without (top) and with (bottom) the cloud. It is hotter in the cloud but colder in the valley.

On Figure 10 ground temperatures are shown with and without the cloud in a zoom region with the finer mesh. It is hotter on the mountain inside the cloud but colder in the valley.

Figure 12 shows the temperature functions of altitude with and without the cloud (with snow) with variable density of air.

4.5 The Chamonix Valley in the Non-Grey Case

As in [8] $\nu \mapsto \kappa_\nu$ is read from the Gemini measurements web site.

To be sure that $\int_0^\infty B_\nu(T) = \sigma T^4$ with a good precision it is necessary to extend $\tilde{\kappa}_\nu$ for $\nu \in (0.01, 0.3$; we set it to be equal to the last available Gemini point.

Then, as shown on Figure 2, $\nu \mapsto \tilde{\kappa}_\nu$ is approximated by the nearest step function that takes only 10 values: $\text{round}(10\kappa)/10$.

As explained above, by this trick we need to compute only 2×10 \mathcal{H} -matrices, even though ν -integrals are computed with 683 quadrature points.

Temperatures at noon with snow and no cloud were computed with the Gemini data of figure 2. Results are shown on the top picture of figure 11.

Then these data were modified in the range $\nu \in (c/18, c/14)$ where κ_ν is set to 1. It simulates grossly the effect of CO_2 which renders the atmosphere opaque in these frequencies. The results are displayed on the middle picture of figure of 11 and on figures 12 and 13. Note that the temperatures are colder.

A similar exercise is made but with κ_ν set to 1 in the range $\nu \in (c/3, c/1.5)$ to simulate an effect in the direction of CH_4 . Results are in the bottom picture of figure 11 and also on figures 12 and 13. Note that the temperatures are hotter. Hence blocking an infrared subrange can either make the day hotter or colder, depending on the position of the subrange, which in these numerical experiments we have childishly called CO_2 and CH_4 . The same observation was made in [8].

On figure 13 the radiation intensities are shown versus wavelength (c/ν) above Chamonix at altitude 3000m.

Note that the computing time is roughly ten time the one with a constant κ because we use a Lebesgue discretization with ten levels.

4.6 Effect of Thermal Diffusion and Wind Velocity

4.6.1 Wind velocity

Convective winds due to temperature differences and modelled by a Boussinesq approximation seem out of simulation reach in areas of several kilometers. On the other hand high atmosphere winds $u_0 \sim 360\text{km/h}$ are numerically tractable if we assume that the effective viscosity is dominated by turbulence, leading to a Reynolds number around 500. Thus the stationary Navier-Stokes equations with fixed varying density are solved in Ω for the scaled velocity \mathbf{u}/u_0 and pressure:

$$\mathbf{u} \cdot \nabla \mathbf{u} + \nabla p - \nu \Delta \mathbf{u} = 0, \quad \nabla \cdot \mathbf{u} = 0, \quad \mathbf{u}(H, y, z) = [0, 1, 0]^T \quad - \quad (25)$$

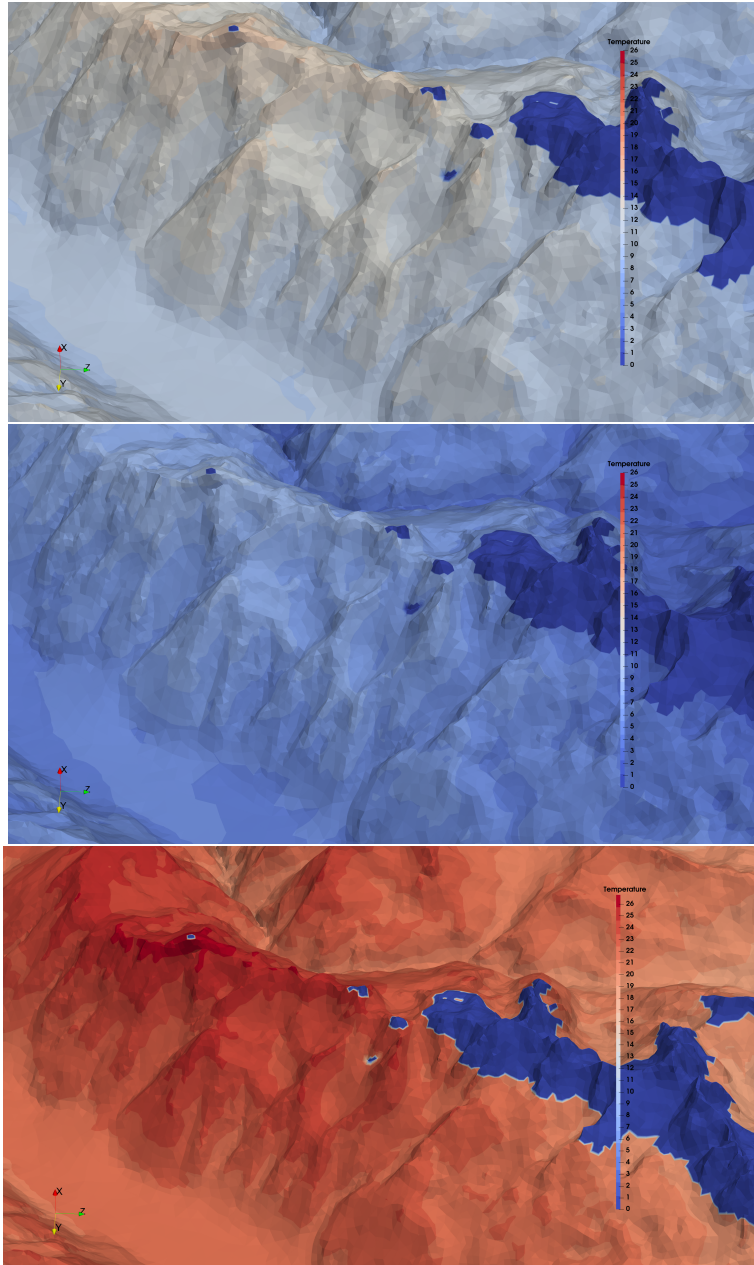


Figure 11: Ground temperatures at noon with snow (no cloud) with κ given by the Gemini data. Below, same situation, but the κ_ν from the Gemini data is put to $1 - x/2$ in the range $\nu \in (c/18, c/14)$ to simulate the absorption by CO_2 . Bottom: same but with $\kappa_\nu = 1 - x/2$, $\nu \in (c/3, c/1.5)$ to simulate the absorption by CH_4 . The color map is the same for all 3. Bluer is colder, browner is hotter.

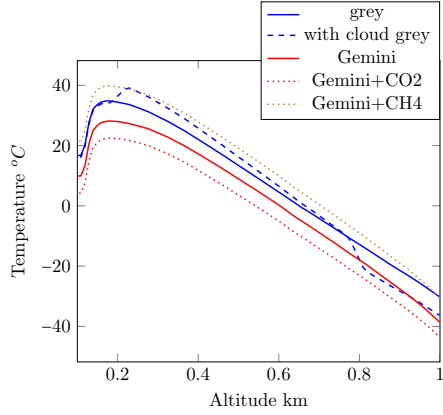


Figure 12: Temperatures versus altitude in the center of the domain computed first with a fixed $\tilde{\kappa}$ with and without the cloud. Then with a variable $\tilde{\kappa}$ (Gemini measurements) with CO_2 or CH_4 corrections.

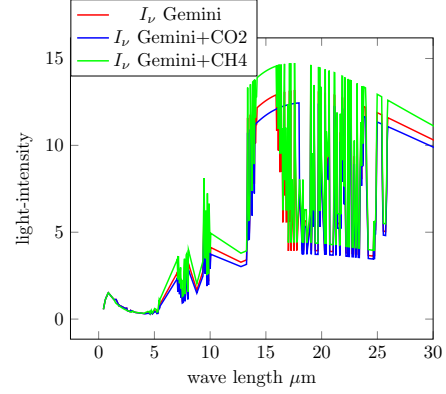


Figure 13: light intensity versus wave length at altitude 3000m in the center of the domain, with Gemini- κ_ν without and with CO_2 or CH_4 corrections.

and Neumann conditions on the remaining boundaries $-\nu\partial_{\mathbf{n}}\mathbf{u} + p\mathbf{n} = 0$. A Newton method is applied to linearize the system and the Taylor-Hood Finite Element method is used for discretization. The linear systems are solved in parallel with the MUMPS library. Less than a dozen iterations are sufficient for convergence in some 600 sec on the M1 (see figure 14)

4.6.2 Simulation of the Temperature Equation

Recall that we have neglected the variations of ρ in the diffusion term:

$$\mathbf{u} \cdot \nabla T - \kappa_T \Delta T = A \int_0^\infty \kappa_\nu (J_\nu - B_\nu(T)) d\nu \text{ in } \Omega, \quad \frac{\partial T}{\partial n} \Big|_{\partial\Omega} = 0.$$

In the computations, the unit length is $L=10\text{km}$. So $\kappa_T = 2 \cdot 10^{-11} [\text{L}]^2/\text{s}$ and $\frac{A}{\rho} = 2.70 \cdot 10^7 [\text{L}]/\text{s}$. In these units $u_0 = 0.01 [\text{L}]/\text{s}$. Let us divide by u_0 :

$$\mathbf{u} \cdot \nabla T - \tilde{\kappa}_T \Delta T = \tilde{A} \int_0^\infty \bar{\rho} \kappa_\nu (J_\nu - B_\nu(T)) d\nu \text{ in } \Omega, \quad \frac{\partial T}{\partial n} \Big|_{\partial\Omega} = 0,$$

where \mathbf{u} is the solution of (25), $\tilde{\kappa}_T = 2 \cdot 10^{-9}$, $\tilde{A} = 5.4 \cdot 10^9$, $\bar{\rho} \kappa_\nu \sim 0.5$.

Evidently if $T^* + \delta T$ is the solution where T^* is the solution with $\mathbf{u} = 0$ and $\tilde{\kappa}_T = 0$, then δT will be very small. This allows for linearization:

$$\mathbf{u} \cdot \nabla \delta T - \tilde{\kappa}_T \Delta \delta T + \delta T \tilde{A} \int_0^\infty \bar{\rho} \kappa_\nu B'_\nu(T^*) d\nu = \tilde{\kappa}_T \Delta \delta T^*.$$

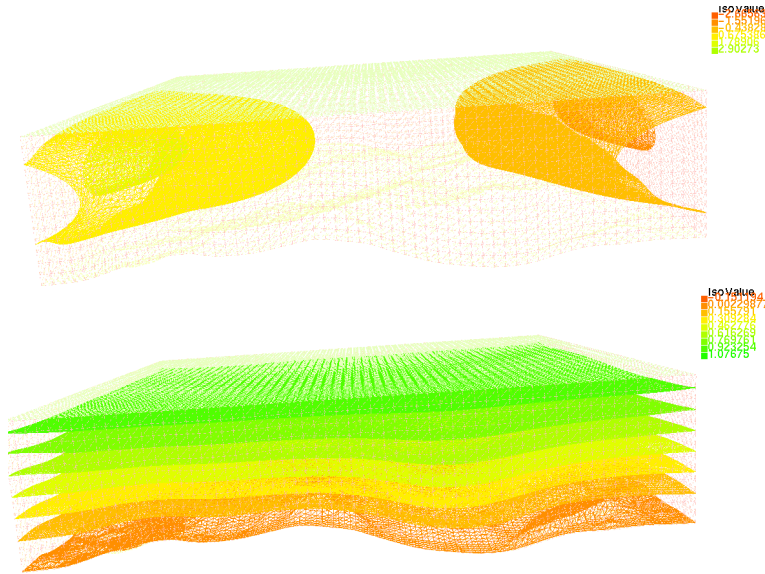


Figure 14: Solution of the Navier-Stokes eqs at $Re=500$. Top: \mathbf{u}_1 , Bottom: \mathbf{u}_2

The PDE is numerically out of reach with the physical values of the parameter. Yet to validate the concept and indicate the trend of the effect of wind and heat diffusion, we have solved it with $\tilde{\kappa}_T = 2 \cdot 10^{-3}$, $\bar{\rho}\kappa_\nu = (1 - x/2)/2$ and $\bar{A} := A' = 5.4 \cdot 10^2$. Notice that if κ_ν does not depend on ν , $A' \int_0^\infty \bar{\rho}\kappa_\nu B'_\nu(T^*) = 4\sigma T^{*3} \bar{\rho}\kappa \sim 1.55$. The results are shown on figures 15, 16.

5 Conclusion

The numerical study validates the claim that heat transfer with radiation can be solved numerically in minutes in 3D on a laptop with $O(100K)$ mesh nodes and a fine resolution of the discontinuities of the absorption parameter in space and frequencies. On a massively parallel supercomputer with $O(1M)$ mesh nodes it can be handled in minutes too.

The method is based on an integral formula for the radiation intensity averaged on the unit sphere of directions. The problem is reduced to an integral equation coupled with the temperature equation with radiation as source. An iterative scheme can be used which is mathematically shown to be convergent and monotone. The numerical errors can be estimated from the difference between the lower and the upper solutions.

A drastic numerical speed-up is obtained when the convolutions in the integrals are replaced by vector products with compressed \mathcal{H} -matrices. Furthermore a small number of matrices are needed only when the integrals are computed as

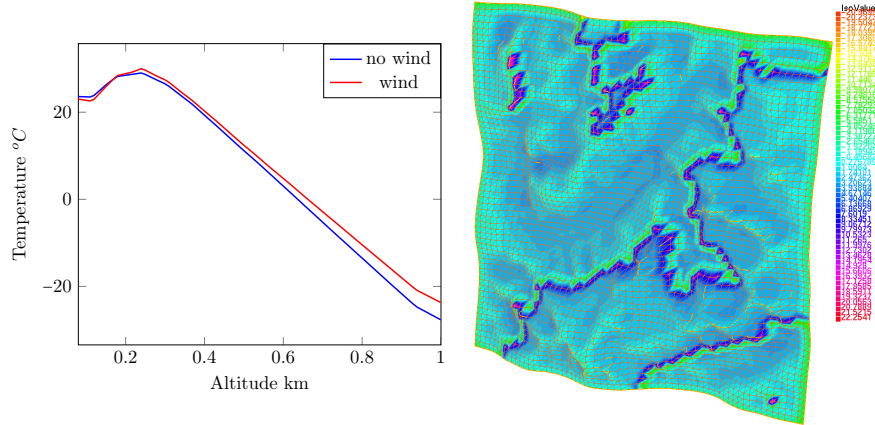


Figure 15: Temperatures versus altitude above Chamonix computed with $\kappa = 0.5(1 - x/2)$, with snow and heat diffusion with and without wind.

Figure 16: Temperature correction δT on the ground due to heat diffusion, $\kappa_\nu = 0.5(1 - 0.5x)$, snow and a small wind.

Lebesgue integrals.

The method was tested on a portion of the atmosphere around the city of Chamonix where high mountains require a full 3D unstructured mesh. The code is precise enough to assert the differences due to changes in κ_ν is a subrange of frequencies. All results seem physically reasonable but we make no climate claim based on the numerical results. Yet we hope to have convinced some to try the code.

6 Acknowledgement

Some computations were made on the machine Joliot-Curie of the national computing center TGCC-GENCI under allocation A0120607330.

The computer code will soon be on github at

<https://github.com/FreeFem/FreeFem-sources/tree/develop/examples/mpi/chamonix.edp>

References

- [1] C. Bardos and O Pironneau. Radiative Transfer for the Greenhouse Effect. submitted to SeMA J. Springer, 2021.
- [2] Craig F. Bohren and Eugene E. Clothiaux. *Fundamentals of Atmospheric Radiation*. Wiley-VCH, 2006.

- [3] R. Cahalan, L. Oreopoulos, A. Marshak, K. Evans, A. Davis, and et al. Bringing together the most advanced radiative transfer tools for cloudy atmospheres. *American Meteorological Society*, 86(9):1275–1294, 2005.
- [4] S. Chandrasekhar. *Radiative Transfer*. Clarendon Press, Oxford, 1950.
- [5] Andrew Fowler. *Mathematical geoscience*. Berlin: Springer, 2011.
- [6] F. Golse and O. Pironneau. Radiative transfer in a fluid. *RACSAM, Springer*, dedicated to I. Diaz(To appear), 2021.
- [7] F. Golse and O. Pironneau. Stratified radiative transfer for multidimensional fluids. *Compte-Rendus de l’Académie des Sciences (Mécanique)*, to appear 2022.
- [8] F. Golse and O. Pironneau. Stratified radiative transfer in a fluid and numerical applications to earth science. *SIAM J. numerical analysis*, To appear, 2022.
- [9] Richard M. Goody and Y. L. Yung. *Atmospheric Radiation. 2nd ed.* Oxford: Clarendon Press, 1996.
- [10] F Hecht. New developments in freefem++. *J. Numer. Math.*, 20:251–265, 2012.
- [11] S.D. Lord. Earth atmosphere transmittance measurements. Technical report, NASA Technical Memorandum 103957,, www.gemini.edu/observing/telescopes-and-sites/sites#Transmission, 1992.
- [12] A. Marshak and A.B. Davis, editors. *3D Radiative Transfer in Cloudy Atmospheres*, volume 5117 of *Physics of Earth and Space Environments*. Springer, 2005.
- [13] F. Ortenberg. Ozone: Space vision. Technical Report nov, Technion, Haifa, 2002.
- [14] O. Pironneau. A fast and accurate numerical method for radiative transfer in the atmosphere. *Compte Rendus de l’académie des sciences (Math)*, December 2021.
- [15] M. Porzio and O. Lopez-Pouso. Application of accretive operators theory to evolutive combined conduction, convection and radiation. *Rev. Mat. Iberoamericana*, 20:257–275, 2004.
- [16] S.Boerm, L. Grasedyck, and W. Hackbusch. Hybrid cross approximation of integral operators. *Numerische Mathematik*, 10(12):221–249, 2005.
- [17] W. Zdunkowski and T. Trautmann. *Radiation in the Atmosphere. A Course in Theoretical Meteorology*. Cambridge Univ. Press, 2007.